

www.acsami.org Research Article

Environmentally Sustainable and Multifunctional Chrome-like Coatings Having No Chromium Designed with Reinforcement Learning

Anwesha Saha, Taigao Ma, Haozhu Wang, and L. Jay Guo*



Cite This: ACS Appl. Mater. Interfaces 2023, 15, 28772-28780



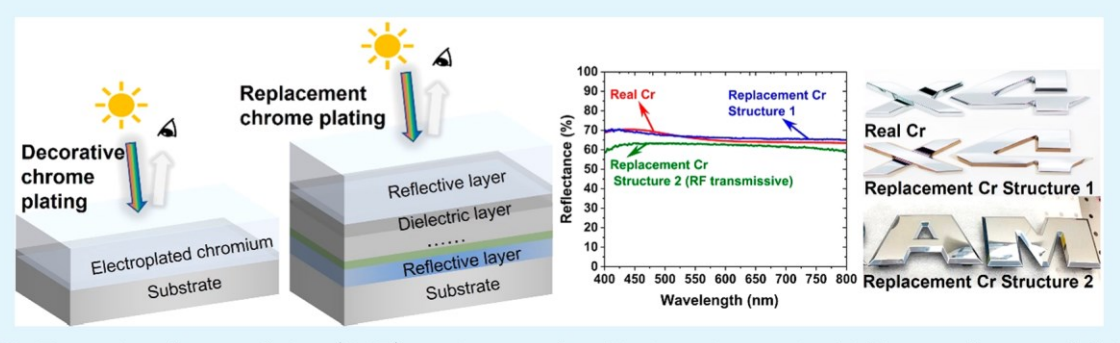
ACCESS

Metrics & More

Article Recommendations

s Supporting Information

in



ABSTRACT: Decorative chrome plating (DCP) continues to be ubiquitous in creating highly appealing metal finishings and coatings, beating out other organic dye-based finishes. However, the hazardous chrome plating process is fraught with adverse health effects for the workers involved and causes significant environmental damage. In this work, we present a multilayer thin film structure to mimic the chrome appearance. To find a design efficiently, we employ a reinforcement learning (RL) algorithm to perform an automatic inverse design. This results in structures composed of environmentally friendly materials that not only have the chrome color but can also achieve additional functions beyond decoration. As an example, one structure is designed to have high transmission in the radio frequency regime, a property that general metals cannot have, which can broaden the decorative chrome applications to include microwave operating devices. The experimental structures are fabricated by physical vapor deposition to demonstrate the indistinguishable chrome color and validate the effectiveness of the RL inverse design approach.

KEYWORDS: chrome replacement, inverse design, structural color, optical coating, reinforcement learning algorithm

■ INTRODUCTION

Optical multilayer thin-film structures are common in many device applications, including solar cells, ^{1,2} OLEDs, ³ filters, ⁴ radiative cooling, ⁵ etc. Thin-film stacks have been extensively used to produce long-lasting structural colors,

the Toyota structural blue, ⁹ in contrast to traditional colors and coatings that are made from organic dyes or colored pigments. One such coating is decorative chrome plating (DCP), a metal finishing process widely used in the industry for coating various automobile parts, kitchen appliances, plumbing fixtures, etc. because of its distinct aesthetic and shiny reflecting appearance.

During the chromium layer deposition process, the plating surface is submerged in a chemical electrolyte containing

ulcers.^{12,13} Toxic emissions containing cadmium and cyanide released during the electroplating process can also lead to air pollution, which could impact the health of millions of people.¹⁴ Given this hazard, there is a significant impetus to find an alternative to replace this process.

Trivalent chromium, Cr(III), is less toxic than Cr(VI) and thus has been considered as an alternative to Cr(VI) for decorative plating applications. However, anodic oxidation of

Cr(VI) is a known human carcinogen and has been found to greatly increase the risk of lung, nasal, and sinus cancer¹¹ workers who are exposed to Cr(VI) mist generated during the plating process. Cr(VI) can also cause severe nasal septum

6-8 ulcerations and perforations, gastritis, and gastrointestinal for example,

hexavalent chromium (Cr(VI)) or trivalent chromium (Cr(III)). The application of a potential difference in the solution results in the transport and subsequent deposition of chromium ions on the object. However, despite offering highly desired properties to the base materials, electroplating chromium is not

Received: March 1, 2023 Accepted: May 21, 2023 Published: June 2, 2023



a sustainable process and causes adverse health impacts that can significantly outweigh its benefits. 10

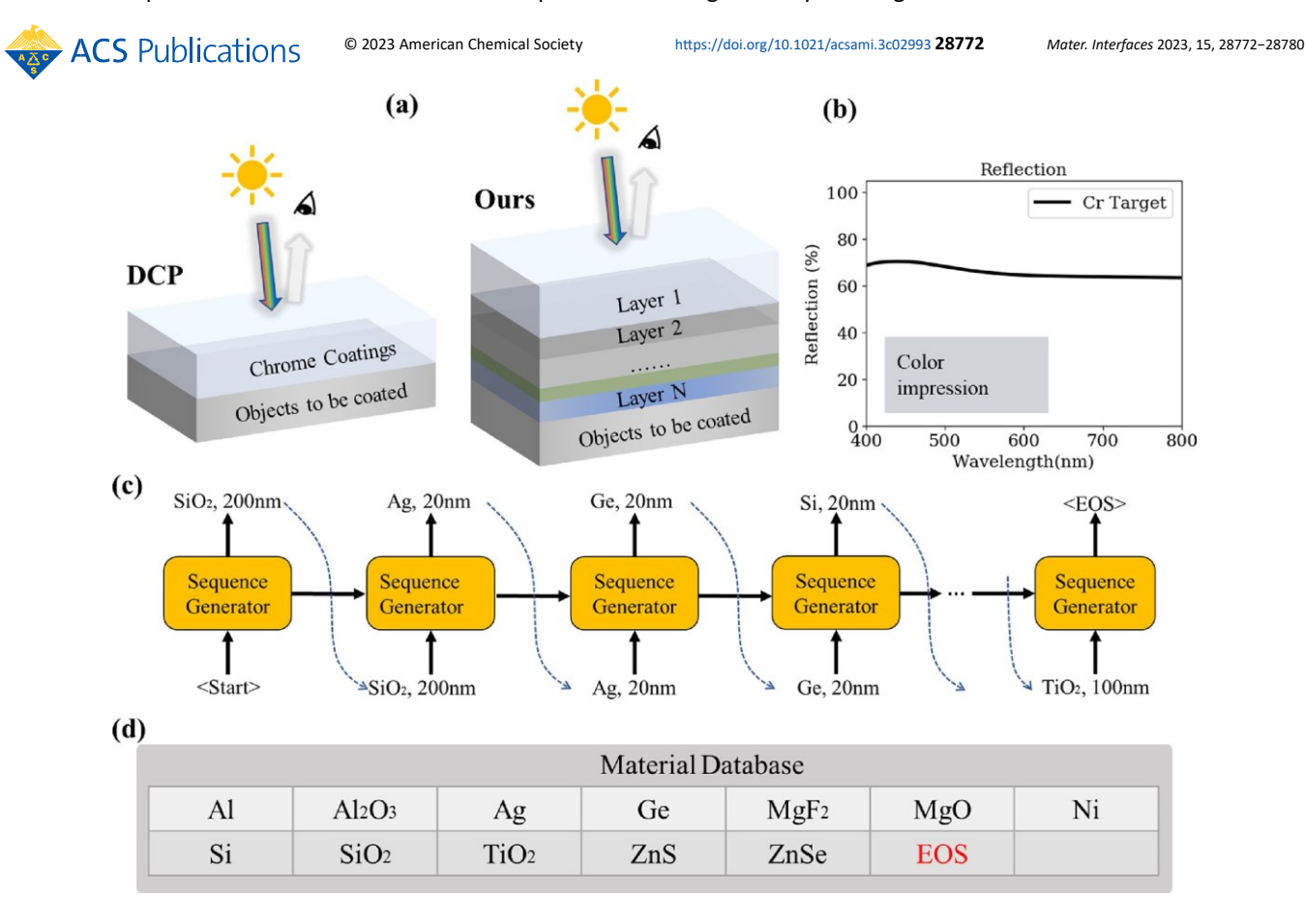


Figure 1. Illustration of the Cr-replacement multilayer stack design. (a) The left schematic shows a normal reflection diagram of a Cr-coated object, and the right schematic shows an N-layer thin-film stack on a glass substrate, which is used to mimic the reflection of the Cr spectrum while excluding Cr from the material selection. (b) Reflection spectrum and visual appearance of a 50 nm Cr layer.³³ (c) Example of the sequential design process used by OML-PPO algorithms. Starting from the first layer, the algorithm outputs the material selection and the corresponding thickness at each layer. The generation process will stop either when the EOS is selected as the material, or the designed stack reaches the maximum number of layers L (we set L = 5). (d) User-defined database used by the RL algorithm to select materials for each layer.

Cr(III) to Cr(VI) and the formation of stable Cr(III) coordinates in aqueous solutions makes the plating process complex due to the need for maintaining a constant pH.¹⁵ Non-electrolytic substitutes for chromium deposition, including high-velocity oxygen-fuel (HVOF) thermal spraying and laser material deposition (LMD),¹⁶ have also been developed. However, both processes still utilize chromium and can use environmentally harmful chemicals.

Further, decorative chromium coatings are often found on vehicle bodies, especially emblems. Despite the attractive appearance, such shiny metal-based emblems block the radio frequency transmission needed for many vehicle sensors. ^{17,18} The US Department of Transportation's

Highway Traffic Safety Administration has National proposed a rule that would require all new light-duty vehicles use vehicle-to-vehicle communication technology. This technology, which relies on the 5.9GHz spectrum, would enable vehicles to communicate with each other and provide a "360-degree awareness" to minimize collisions and accidents. 19,20 For this, it would be desirable to eliminate the use of chromium (metal) in the plating process while still preserving its attractive appearance. In this work, we propose and demonstrate multilayer thin-film stacks deposited by physical vapor deposition that can mimic the visual appearance of Cr(VI)-plated objects but without using any chromium. One of the structures is designed to be

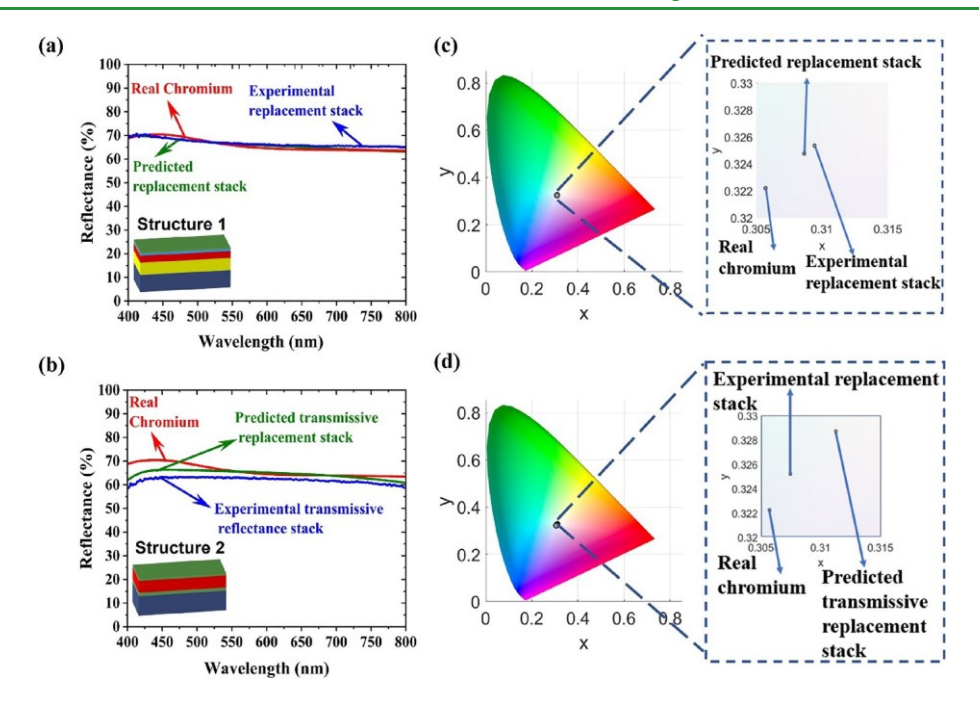


Figure 2. (a) Structure 1 (S1) shown in inset (bottom left): diagram representing the four-layer replacement Cr stack involving 19 nm Ge (green)/ 17 nm TiO₂ (sky blue)/82 nm SiO₂ (red)/139 nm Ni (yellow) on a glass substrate (dark blue). (b) Structure 2 (S2) shown in the inset (bottom left): diagram representing the three-layer RF transmissive replacement structure involving 21 nm Ge (green)/119 nm SiO₂ (red)/33 nm Ge (green) on a glass substrate (dark blue). The plots in (a) and (b) show a comparison of the reflection spectra of the 50 nm thick chromium layer (red)³³ and the predicted (green) and experimentally deposited (blue) replacement chrome stacks for (a) S1 and (b) S2, respectively. A zoomed-in view of the reflectance spectra in the 60–80% region of S1 can be found in the Supporting Information (Figure S4). The plots on the right show a comparison of the literature Cr color, predicted color, and experimentally obtained color of the replacement stacks plotted on the relative CIE 1931 coordinates for (c) S1 and (d) S2, respectively. The magnified views in (c) and (d) show how close the three colors are.

transmissive in the radio frequencies (RF) while retaining the metallic appearance of chromium, which enables the extension of DCP to RF applications. This presents an environmentally sustainable approach to produce attractive metallic-looking coatings.



METHODS

To design a thin-film structure that can produce the desired chromium reflection spectrum, we formulate the task as an inverse design problem.²¹ In this case, we design multilayer structures to achieve a certain optical response, namely, the reflection spectrum. However, the design process can be non-trivial because for each layer, both material selection and thickness need to be considered. The wavelength-dependent nature²² of the refractive index of a material can worsen this situation when designing in a broadband wavelength region, e.g., the whole visible region in this case. To make this easier, many optimization-based methods have been devised to design thinfilm structures, including needle optimization,²³ particle swarm optimization (PSO),²⁴ genetic algorithms,²⁵ etc. However, these methods are usually based on heuristic searching without learning from experience, which can lead to suboptimal performance. Additionally, as the number of layers in the design increases, the search space for the structures

increases exponentially, which makes the search for good designs inefficient and challenging. Recently, many machine learning-based methods have been proposed that demonstrate good performance for inverse design.^{26–31} In this work, we use a reinforcement learning (RL) algorithm that we developed previously:³² Optical MultiLayer-Proximal Policy Optimization (OML-PPO), which learns from its past results when searching within a large space.

In this inverse design problem, our target is to produce the same reflection spectrum as that of chrome-coated objects. The method is generally applicable to generate a multilayer structure to produce any target optical response,²⁷ an example of which is provided in the Supporting Information (Figure S1 shows a replacement structure that can produce the same reflection spectrum as that of gold). We begin by initializing the algorithm with the target reflectance spectrum of the coating that we are interested in replicating. Then, for a multilayer thin-film structure as shown on the right in Figure 1a, each layer can be expressed as $s_i = [m_i, d_i]$, where m_i is the material selection and d_i is the corresponding thickness at the Ith layer. We can use the sequence S = $\{s_1, s_2, ..., s_N\}$ = $\{[m_1, d_1], [m_2, d_2], ..., [m_N, d_N]\}$ to describe the overall thin-film structure, where N is the total number of layers. Therefore, designing such a structure is to find a specific sequence of material and thickness combination that gives the desired target optical response. Reinforcement learning does well with such sequential generation.³² The design steps that OML-PPO uses are represented in Figure 1c. For the Ith layer, the RL algorithm takes the designed layers from previous steps and predicts the material m_l and thickness d_i sequentially. This design process automatically stops when the designed stack reaches the maximum number of layers L (here we set L = 5). At each step, the material m_l is selected from a list of materials in the user-created database as shown in Figure 1d. Twelve materials (both dielectrics and metals) were included in the database for the design based on their availability, non-toxicity, and ease of deposition. The refractive indices of these materials deposited by PVD were experimentally measured by using spectroscopic ellipsometry and are provided in the Supporting Information (Figure S2). We also have one faux material that is used as an indicator of the end-of-sequence (EOS). Once the algorithm selects the EOS, the design process stops immediately irrespective of whether the designed structure has reached the maximum number of layers. This can be used to design structures with a variable number of layers (for example, 3, 4, and 5 layers when L = 5). We set the layer thickness to be in the range of 5 to 250 nm, discretized by a 5 nm gap (corresponding to 50 thickness selections in total). In this way, the total search space spans across 10^{14} different combinations of structures ((13 materials \times 50 thickness selections)5), which is an incredibly challenging task for traditional optimization methods to deal with.

To simplify the task, we only consider the normal reflection in the visible range and set the design target to be the Cr reflection spectrum R_t , which is shown in Figure 1b.³³ The inset figure in Figure 1b also shows an example of the shiny reflective Cr color. The transfer matrix method (TMM) is used to simulate the reflection spectrum R_d of the layered structure. During the design process, the difference between the designed spectrum R_d and the target spectrum R_t is minimized. Since the RL algorithm learns to design multilayer structures by maximizing the reward, we define the reward G_t to be 1 minus the spectrum difference and express it as:

$$G_{t=1} - \frac{1}{n} \sum_{i}^{n} (R_{t}(S, \lambda_{i}) - R_{d}(S, \lambda_{i}))^{2}$$

 $_{i=1}$ (1) where λ_i is the wavelength, which ranges from 400 to 800 nm with 5 nm increments. After the design process, we select the best-discovered structure and use PSO to further fine-tune the thickness at each layer, which can eliminate the influence of thickness discretization and improve the performance of the prediction. The fine-tuned structure is then the final design. More details about this design process can be found in ref 32.



RESULTS AND DISCUSSION

Using the RL algorithm described in the methods, we designed several structures as potential replacements for DCP, of which we chose to experimentally deposit two for ease of fabrication. Several other designed structures with simulation results can be found in the Supporting Information (Figure S3). We denote the two selected structures as "Structure 1" (S1) and



Figure 3. Photos of replacement chrome coated plastic substrates. (a) Comparison between a commercially coated chromium finish on ABS substrates in the shape of "x 4" used in automobiles (top) and ABS substrates coated using S1 (bottom) taken at a 45° angle. (b) ABS plastic pieces coated with the RF transmissive replacement chrome design (S2) taken at a 60° angle. (c) PVD chrome (top), replacement stack S1 (middle), and green hue replacement chrome stack S1' (bottom) coated on ABS plastic pieces taken at a 45° angle.

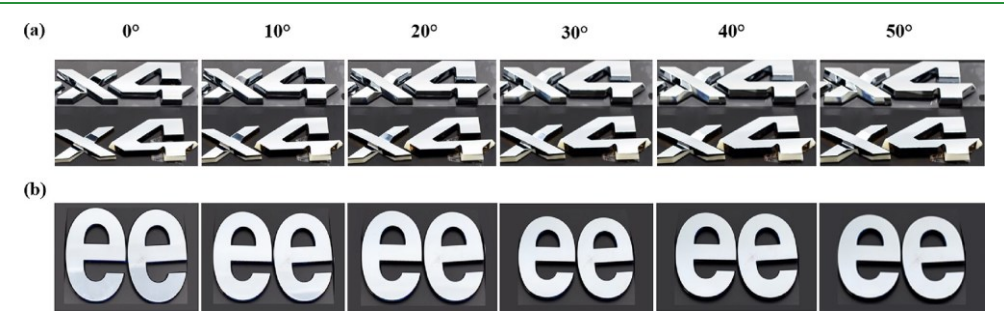


Figure 4. Angular views of the replacement coatings. (a) Photos of the samples with angled views (0–50°). They include real chrome (top) and S1 (bottom) on ABS substrates. (b) S2 on ABS substrates, showing that the chromium appearance can be maintained over a wide viewing range.

"Structure 2" (S2), as illustrated in the insets of Figures 2a and 2b, respectively. Going from top to bottom, S1 includes Ge (19 nm)/TiO₂ (17 nm)/SiO₂ (82 nm)/Ni (139 nm)/glass substrate and S2 includes Ge (21 nm)/SiO₂ (119 nm)/Ge (33 nm)/glass substrate. Since there are no metals in S2, it can potentially allow high transmission in radio frequencies, providing a multifunctional property to DCP for microwave applications, which will be discussed later. We experimentally deposited these two structures using electron beam evaporation, the details of which can be found in the Experimental Methods section at the end.

Figures 2a and 2b, respectively, show the predicted (green) and measured (blue) reflection spectra of S1 and S2 at normal incidence. The spectrum was measured using a normal incidence spectrometer. For a better comparison, the reflection spectrum of real Cr (red) at normal incidence³³ is also shown in each figure. Chromium has a broadband reflection spectrum across the optical wavelength range. For both structures, the predicted and measured spectrum show a broadband reflection trend, which agrees very well with the actual Cr spectrum. For S1, the three spectra overlap with each other, so a zoomed in view of the spectra in Figure 2a is shown in the Supporting Information to magnify the minimal differences (Figure S4). In Figure 2b, for S2, we find that while the predicted and

measured spectra trends agree well, the reflection values differ somewhat. These discrepancies in the experimental results can be attributed to slight thickness variations during deposition.

However, these small differences in the reflectance of the predicted and experimental stacks compared to real chromium do not impact the overall color appreciably. In Figure 2c,d, we compare the combined RGB data from the predicted, measured, and real chrome spectra on the CIE 1931 chromaticity plots for S1 and S2, respectively. All three colors overlap well for both structures and lie in the middle of the CIE plot, indicating Cr color as desired. In each figure, the expanded view of the CIE color map further demonstrates that the differences between the colors in the three spectra are minimal.

Since the design target is reflection and there is no light transmitting through the bottom layer, the chrome-mimicking color can be produced on different substrates as long as film deposition on the substrate is feasible. We show the robustness of the design by depositing the same chrome-mimicking structure on other types of substrates, e.g., ABS plastic, which is widely used in many practical applications. An example of this is demonstrated by depositing the replacement stack on top of ABS plastic pieces that are often used as markers on the back of

automobiles such as "4 x 4", or company logos like "Jeep". Figure 3a shows a comparison of ABS plastic pieces (the letters "x 4") coated using either a commercially coated chromium finish (top) or the replacement stack S1 (bottom). Visually, one can observe that the replacement stack S1 is very similar to the commercially coated Cr. The edges of the "x 4" pieces coated with S1 show the color of the bare ABS plastic, and a magnified view is shown in Supporting Information Figure S5. The edges of this sample are bare because they were covered by tape during sample mounting, but the mounting process was improved, and the pieces coated subsequently did not have this effect as seen in Figure 3b. Figure 3b shows a sample of black ABS plastic coated with replacement stack S2, which appears to be visually similar to a real Cr coating while having the added advantage of being RF-transmissive.

We would like to note one unique feature of our

with a green hue S1' (bottom). The bottom structure, S1' in Figure 3c, consists of a stack of Ge (8 nm)/SiO₂ (139 nm)/Ni (138 nm) on a glass substrate, which is fine-tuned from S1. Figure 3c also demonstrates a color difference between a PVD-based Cr coating and our replacement stack. Using an evaporation-based alternative process to deposit a chromium-like finish is more desirable since PVD chromium renders a color that is significantly darker than electrodeposited chromium.

Apart from substrate independence, our replacement coatings are also angle-independent, just like real DCP coating. Figure S6 shows the simulated angle-resolved reflection spectrum of the two design structures (S1 and S2) and chrome. At viewing angles of up to 50°, the reflection always exhibits a flat spectrum with an amplitude that is consistently between 60 and 70%. This angle robustness is also observed when using ABS substrates. Figure 4a shows

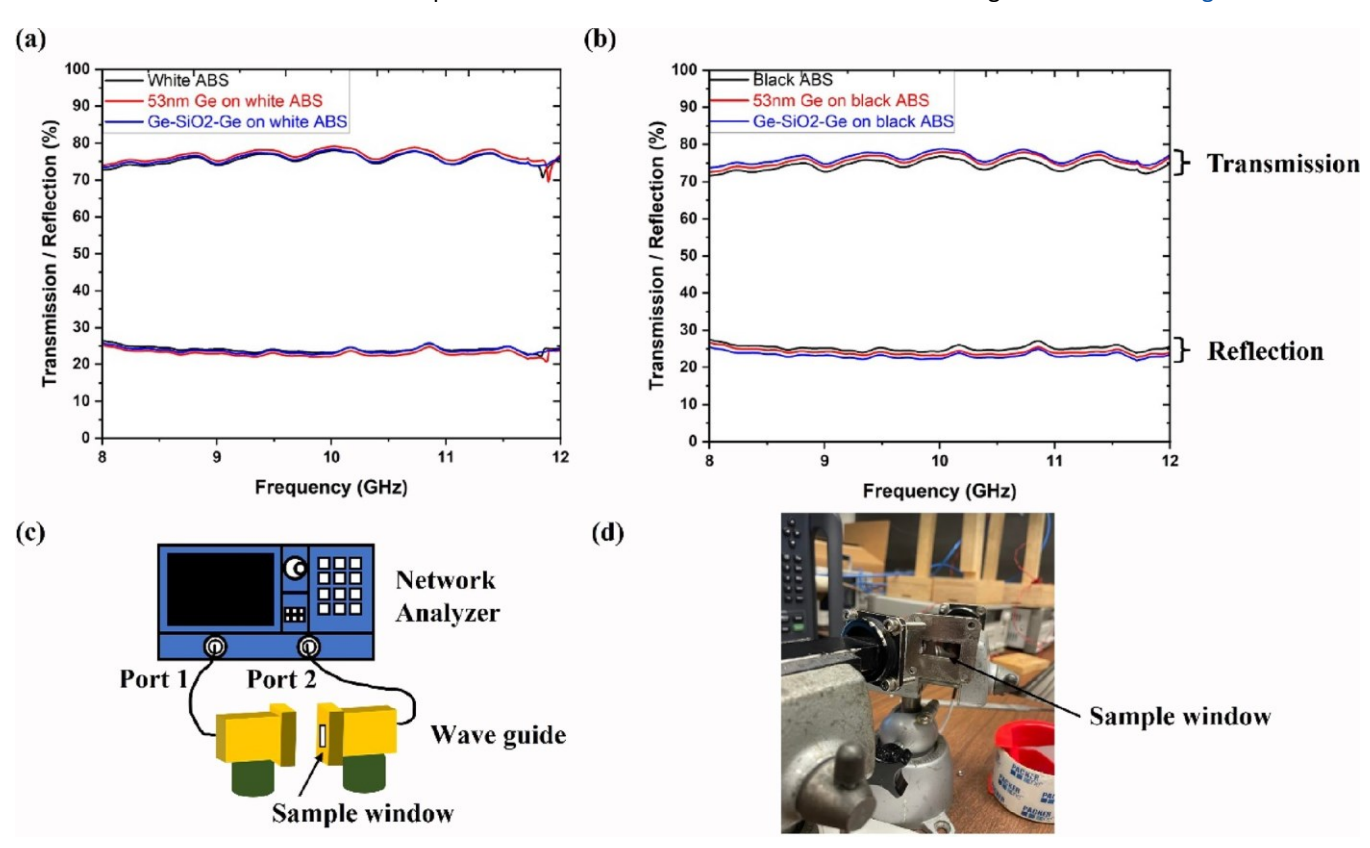


Figure 5. RF transmission and reflection measurements in the range of 8–12 GHz frequencies. The transmission and reflection of S2 on (a) 2.6 mm white ABS plastic substrate and on (b) 3 mm black ABS plastic. As a comparison, for each substrate, we measured the transmission and reflection of a pristine substrate, 53 nm Ge, on the substrate and S2 coated on the substrate and found the transmission to remain the same. (c) Schematic showing the measurement setup with the waveguide and ports labeled in the setup. (d) Picture of the waveguide cross section in which the samples were handcrafted to fit into.

approach, which is that we can easily create different "tones" of chrome color by adjusting the stack parameters. In Figure 3c, we show the appearance of a piece of ABS plastic coated with PVD chrome (top), one with replacement stack S1 (middle) and another with the replacement stack

pictures taken of the real chrome (top) and S1 (bottom) coated on ABS substrates at different viewing angles. Figure 4b shows S2 coated on the ABS plastic pieces. The angle varies from 0 to 50°, and we can see that the appearance is consistent with that of chromium. An additional set of

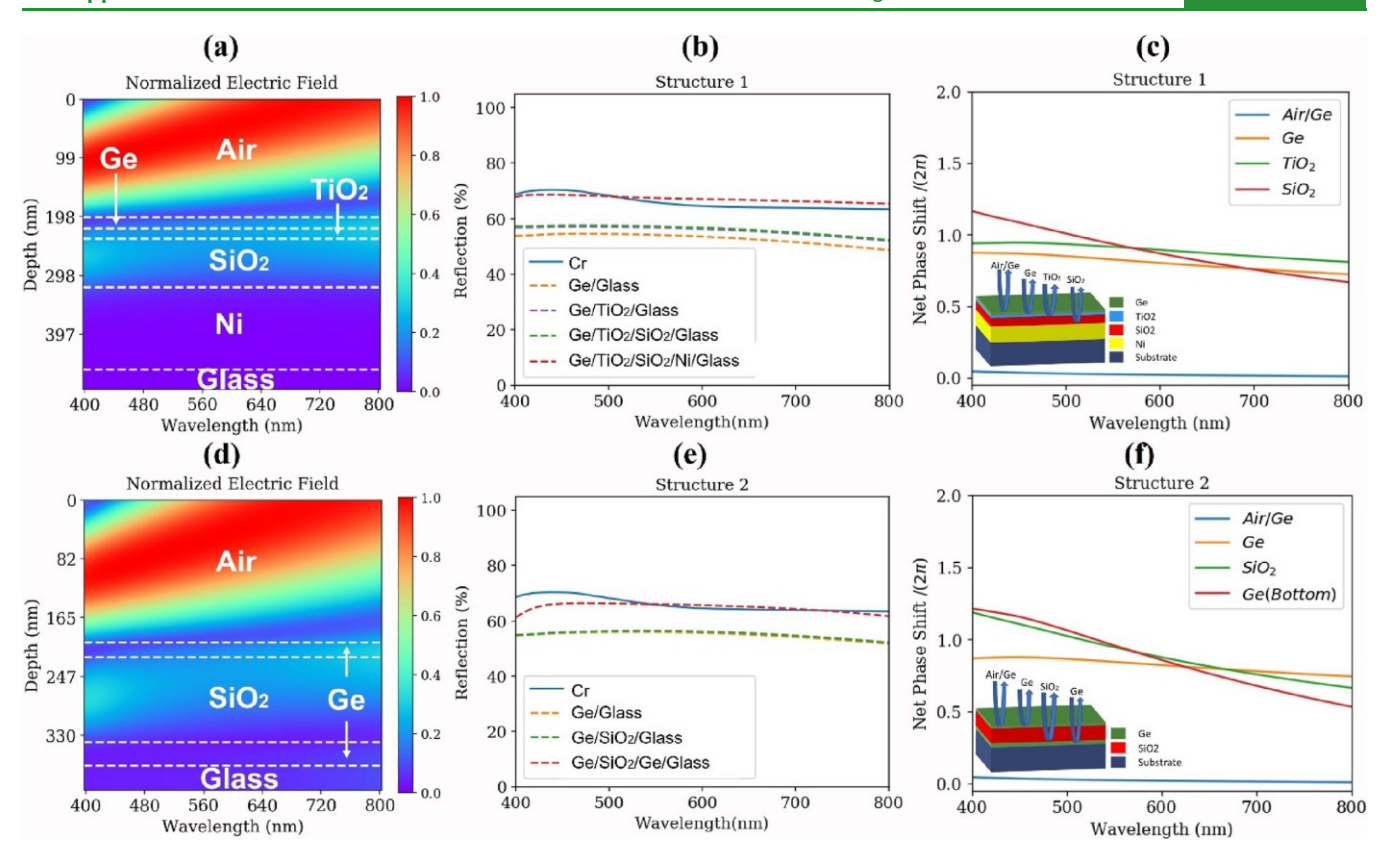


Figure 6. Electric field distribution of (a) S1 and (d) S¹. The strong electric field in air over the whole visible range indicates that the structure has a flat spectrum with high reflection. (b) and (e) show the step-by-step reflection analysis for S1 and S2, respectively. (c) and (f) show the net phase shift at each layer for S1 and S2, respectively. The net phase shift from each component balances each other, leading to constructive interference and an overall increase in the reflection compared to a single Ge layer.

pictures are included in the Supporting Information (Figure S7), in which a reference object is placed alongside the coated piece to demonstrate the angle variation and the color consistency across the viewing angles presented in this section (0 to 50°).

Multifunctionality in the RF Region. Commercial DCPcoated objects block RF signals because metals (chrome in DCP) are highly reflective in such frequencies. Thus, they are seldom used in RF-based devices, e.g., automobile radars. Semiconductor materials such as Ge have much smaller losses in the RF regime, ^{34,35} so we designed S2, another chromemimicking stack that has high transmission in the RF regime simultaneously, as the structure involves thin layers of Ge and SiO₂ only. To demonstrate this, we experimentally measured the transmission and reflection of S2 in the range of 8–12 GHz as shown in Figure 5. This was done by using a WR90 waveguide to accommodate such frequencies and a Keysight network analyzer for measurement. The measurement setup is shown in Figure 5c, and the waveguide is in Figure 5d. The sample was

Supporting Information (Figure S8). Thus, our results suggest that the designed S2 is a multifunctional coating that yields a similar appearance as DCP while providing high

medium. In a multilayer structure, there are multiple reflections in each layer, and the light reflected from the top and bottom surface of each layer interfere. Based on the

handcrafted to fit into the cross section of the waveguide with the coated sides facing port 1. The structure was deposited on two types of ABS plastic: white (2.6 mm thick) and black (3 mm thick). For each substrate, we tested the RF transmission of (1) the substrate without any coating, (2) the substrate coated with a 53 nm layer of Ge (the combined thickness of the two Ge layers in S2), and (3) the substrate coated with S2. By analyzing the S-parameters (S21 for transmission from port 2 to 1 and S11 for reflection back to port 1), we found that the transmission and reflection remain very close to that of a pristine substrate and are independent of the substrate used as shown in Figure 5a,b. The ripples in the measured data are due to frequencymatching calibration errors. We also tested RF transmission through glass substrates coated with S2 similarly, and the results can be found in the

 $^{^{1}}$ nd, where λ is the wavelength of light. Additionally, a reflection phase shift of π is introduced when the refractive index of the incident medium is less than the transmitting

transmission in the RF region, which is impossible using traditional metalbased chrome coatings.

Analysis. In Figures 6a and 6d, we map the normalized electric field intensity for S1 and S2, respectively. The strong electric field in air across the whole visible range indicates the high broadband reflectance of both structures. When light travels from one medium to another, there are three phenomena that occur: reflection, transmission, and absorption. The reflection coefficient (r), which is the proportion of light that gets reflected at the interface of two media, depends on the refractive indices $(n_1$ and $n_2)$ and can be obtained from

Fresnel's equations: $r = \begin{vmatrix} n_1 - n_2 \\ n_1 + n_2 \end{vmatrix}$ at normal incidence from medium 1 to 2.

The overall reflection from a multilayer structure also depends on the thickness of each layer in addition to the refractive index (n). This is because reflection has two components, amplitude (r) and phase (ϕ) . The thickness (d) of the medium through which light is transmitted adds on a propagation phase, which can be simply expressed as difference in phase of the reflected light, constructive or destructive interference can occur. With this in mind, we can analyze the mechanism by which the proposed multilayer structures have a high broadband reflection.

To begin, both our structures have Ge as the topmost layer. Having a high refractive index material in the top layer (Ge), a significant portion of the light is reflected off the top layer itself. The remaining light transmits through after some absorption loss in Ge, as shown in Figure S9. However, to achieve a chrome look, we need ~70% broadband reflection, so we need the subsequent layers to reflect the transmitted light strongly and with a phase such that all the reflections can interfere constructively. In S1, the next two layers are dielectrics, TiO2 and SiO2. Dielectric materials do not reflect or absorb strongly, as is evidenced by the minimal increase in reflection in the Ge/TiO₂/SiO₂/glass structure (green dashed curve) compared to the Ge/glass structure (orange dashed curve) in Figure 6b. These layers only add a propagation phase, and most of the light gets transmitted on to the next layer, which is nickel in this case. Figure 6c shows the net phase shift (scaled by 2π) in each layer, which is a combination of the reflection phase and the propagation phase discussed above. We can see that the net phase added on to the transmitted wave remains close to 2π (the green and red curves are close to 1 in the net phase shift/ 2π plot) across wavelengths, which ensures that there will be constructive interference in the reflected waves. Interestingly, at wavelengths below 550 nm, the phase shift due to SiO_2 is slightly higher than 2π , and beyond that, the phase shift dips below 2π . This is compensated by the lower (lower than 2π) accumulated phase in the Ge and TiO₂ layers

at wavelengths below 550 nm and higher (higher than 2π) phase at wavelengths above. Finally, the Ni layer acts as a reflective mirror that boosts the reflection coefficient to increase the overall reflection from 50 to 70% as seen from the red dashed line in Figure 6b. The cumulative effects of the reflection coefficient boosts due to constructive interference leads to the high broadband reflectance that is characteristic of chrome.

A similar phenomenon is the reason behind the overall broadband reflection from S2. As seen in Figure 6e, the top Ge layer has a large reflection (orange dashed curve for Ge/glass structure), and it does not change due to the SiO₂ (notice that the green dashed curve for Ge/SiO₂/glass overlaps with the orange). The dielectric SiO2 layer adds a phase to the transmitted light that is slightly above 2π below 550 nm and dips below 2π at wavelengths above 550 nm as shown in Figure 6f. This decrease in the phase at 800 nm and above can be attributed to the slight dip in the overall reflection (blue solid curve) from this structure at longer wavelengths as seen in Figure 6e. This does not feature in the overall reflection from the structure at the shorter wavelengths (400-750 nm) because the decrease in phase due to the SiO₂ is compensated by the phase due to the top Ge layer, which remains at a constant $\sim 2\pi$. Finally, the bottom Ge layer, with its high refractive index, enhances the reflection. The red dashed line in Figure 6e shows the reflection spectrum from S2 and we can see that the total reflection is ~70% across all wavelengths. Thus, in both structures, adding the dielectric materials make the net phase shift close to 2π , which leads to constructive interference that increases the overall reflection to produce a Cr-like spectrum.



CONCLUSIONS

In this work, we propose two novel structures for DCP replacement based on multilayer thin films, offering a visual appearance identical to that of real Cr, completely eliminating the harmful Cr electroplating process. The structures are designed by the OML-PPO algorithm based on reinforcement learning. Two of many RL-designed structures were fabricated, and their visual resemblance to Cr coatings was demonstrated. The structures are robust to a wide viewing angle and a variety of substrates. Multifunctionality can be designed into the target response, for example, one structure exhibits high transmission in the RF region, a function that general Cr coatings cannot have. We believe that our work can point out a method for machine learning-assisted multilayer thin-film design that can provide sustainable and multifunctional properties, which has not been explored in most work in this field.

EXPERIMENTAL METHODS

Structure Selection. The algorithm generated several multilayer structures that would all give the same desired target optical response, namely, the chrome look. A few of these structures have been shown in the Supporting Information (Figure S3), and some can be found in our previous work.²⁷ Of these, we chose structure 1 and structure 2 for fabrication and demonstration in this work for two primary reasons: ease of availability of the materials and the ability to complete the fabrication in one evaporation chamber. We picked structures with materials that were readily available in the same evaporator in our cleanroom facility to minimize the workflow transitions between multiple chambers. This helped us fabricate the structures with ease and as fast as possible. If any of the materials that were chosen for fabrication in this work are cost-limiting, we can just as easily use a different structure that involves more cost-effective materials. As an example, an RF-transmissive replacement chrome structure that uses amorphous silicon (more cost effective) instead of germanium was generated and is included in the Supporting Information (Figure S10).

Electron Beam Evaporation. Each of the layers used in the replacement stack were individually evaporated on a 0.5 mm thick piece of silicon wafer in an Angstrom Engineering Evovac Evaporator. For S1, the desired thickness for the bottom metal layer, Ni, was 138 nm with a deposition rate of 4 Å/sec. SiO_2 (82 nm) was deposited at a rate of 3 Å/sec, TiO_2 (18 nm) was deposited at 2 Å/sec, and Ge (17 nm) was deposited at 2 Å/sec. For S2, the Ge and SiO_2 were deposited at the same rates as in S1.

Material Characterization. The J. A. Woollam M-2000 was used (wavelength range: 400–1600 nm, three angles of incidence: 65, 70, and 75°) for spectroscopic ellipsometry to measure the thickness of the evaporated films. This was also used to determine the optical constants such as the real and imaginary parts of the refractive index of the films. A B-spline model was used for fitting data from metals and dielectrics. Reflectance spectra were measured using a portable normal incidence spectrometer integrated with a white light source. It included an HR4000 Ocean Optics high resolution spectrometer, and the data was acquired using the SpectraSuite software.

TMM Simulation. A MATLAB simulation based on the transfer matrix method was used to verify the prediction from the machine learning algorithm and the experimental data obtained. Optical constant data for the materials were obtained using ellipsometry.

RF Measurements. The RF measurements were conducted with the use of a Keysight network analyzer, model E5080B-2KO, and a set of waveguides in the WR90 size (width: 22.86 mm, height: 10.16 mm) covering a frequency range of 8.2 to 12.4 GHz. The setup was calibrated using three calibration loads: a short (a flat metal plate), an offset short (flat metal plate with a little bit of waveguide pipe before the flat part), and a matched load (no reflections). These calibration loads were made in-house in the RF measurement laboratory.



ASSOCIATED CONTENT

* Supporting Information

The Supporting Information is available free of charge at https://pubs.acs.org/doi/10.1021/acsami.3c02993.

Refractive index for the materials used in the design, few other structure designs generated using the algorithm, RF reflection and transmittance of the RF-transmissive structure on glass substrate, and the simulated absorption of visible light inside both the structures discussed in this paper (S1 and S2) (PDF)



AUTHOR INFORMATION

Corresponding Author

L. Jay Guo – Department of Applied Physics and Department of Electrical Engineering and Computer Science, University of

Michigan, Ann Arbor, Michigan 48109, United States;

orcid.org/0000-0002-0347-6309; Email: guo@ umich.edu

Authors

Anwesha Saha – Department of Applied Physics, University of

Michigan, Ann Arbor, Michigan 48109, United States;
orcid.org/0000-0002-3430-3937

Taigao Ma – Department of Physics, University of Michigan, Ann Arbor, Michigan 48109, United States

Haozhu Wang – Department of Electrical Engineering

Computer Science, University of Michigan, Ann Arbor, Michigan 48109, United States

Complete contact information is available at: https://pubs.acs.org/10.1021/acsami.3c02993

Author Contributions

A.S. and T.M. contributed equally to this work.

Funding

This work has been supported by the Michigan Translational Research & Commercialization (MTRAC) program and the National Science Foundation under grant no. PFI-2213684.

Notes

The authors declare the following competing financial interest(s): The structures presented in this study are the subject of an IP disclosure to the University of Michigan IP office.

(Haozhu Wang) Work done while at University of Michigan. Currently at Machine Learning Solutions Lab, Amazon Web

Services.

A US provisional patent application has been submitted based on the work described in this paper.



ACKNOWLEDGMENTS

Portions of this work were performed at the Lurie Nanofabrication Facility, which is supported by the College of Engineering at University of Michigan. We also especially acknowledge the contributions of Kaleo Roberts, PhD candidate in the EECS department at the University of Michigan, for his help with the RF transmission measurements presented in this work. We want to thank Silvia Cardarelli from the EECS department at the University of Michigan for her help with taking the photographs used in Figures 3 and 4 in this manuscript.



REFERENCES

- (1) Agrawal, M.; Peumans, P. Broadband Optical Absorption Enhancement through Coherent Light Trapping in Thin-Film Photovoltaic Cells. *Opt. Express* 2008, *16*, 5385–5396.
- (2) Morales-Masis, M.; Wolf, S. D.; Woods-Robinson, R.; Ager, J. W.; Ballif, C. Transparent Electrodes for Efficient Optoelectronics. *Adv. Electron. Mater.* 2017, *3*, 1600529.
- (3) Zou, S.-J.; Shen, Y.; Xie, F.-M.; Chen, J.-D.; Li, Y.-Q.; Tang, J.-X. Recent Advances in Organic Light-Emitting Diodes: Toward Smart Lighting and Displays. *Mater. Chem. Front.* 2020, *4*, 788–820.
- (4) Yang, C.; Ji, C.; Shen, W.; Lee, K.-T.; Zhang, Y.; Liu, X.; Guo, L. J. Compact Multilayer Film Structures for Ultrabroadband, Omnidirectional, and Efficient Absorption. *ACS Photonics* 2016, *3*, 590–596. (5) Raman, A. P.; Anoma, M. A.; Zhu, L.; Rephaeli, E.; Fan, S. Passive Radiative Cooling below Ambient Air Temperature under Direct Sunlight. *Nature* 2014, *515*, 540–544.
- (6) Li, W.; Shi, Y.; Chen, Z.; Fan, S. Photonic Thermal Management of Coloured Objects. *Nat. Commun.* 2018, *9*, 4240.
- (7) Stavenga, D. G. Thin Film and Multilayer Optics Cause Structural Colors of Many Insects and Birds. *Mater Today Proc* 2014, *1*, 109–121.
- (8) Rorem, B. A.; Cho, T. H.; Farjam, N.; Lenef, J. D.; Barton, K.; Dasgupta, N. P.; Guo, L. J. Integrating Structural Colors with Additive Manufacturing Using Atomic Layer Deposition. *ACS Appl. Mater. Int.* 2022, *14*, 31099–31108.
- (9) Mehta, A. Structural Colour. Chemistryworld. May 25, 2018, updated May 25, 2018. https://www.chemistryworld.com/features/ structural-colour/3009020.article (accessed 2023-02-18).
- (10) Baruthio, F. Toxic Effects of Chromium and Its Compounds. *Biol. Trace Elem. Res.* 1992, *32*, 145.
- (11) Lieberman, H. Chrome Ulcerations of the Nose and Throat. *New Engl. J. Med.* 1941, 225, 132–133.

- (12) Lindberg, E.; Hedenstierna, G. Chrome Plating: Symptoms, Findings in the Upper Airways, and Effects on Lung Function. *Archives Environ. Heal. Int. J.* 1983, *38*, 367–374.
- (13) Community Information Sheet. *Reducing air pollution from:* Electroplating operations. https://www.epa.gov/sites/default/files/ 2017-06/documents/electroplating_comm_info.pdf (accessed 202302-18).
- (14) Schopphoven, T.; Gasser, A.; Wissenbach, K.; Poprawe, R. Investigations on Ultra-High-Speed Laser Material Deposition as Alternative for Hard Chrome Plating and Thermal Spraying. *J Laser Appl* 2016, *28*, No. 022501.
- (15) Handy, S. L.; Oduoza, C. F.; Pearson, T. Theoretical Aspects of Electrodeposition of Decorative Chromium from Trivalent Electrolytes and Corrosion Rate Study of Different Nickel/Chromium Coatings. *Trans. Imf* 2006, *84*, 300–308.
- (16) Green laser alternative to prohibited hard chrome plating. August 15, 2017, updated August 15, 2017. https://optics.org/news/8/8/26. (accessed 2023-02-18).
- (17) Hossain, E.; Mamun, N.; Faisal, M. F. Vehicle to Vehicle Communication Using RF and IR Technology. 2017 2nd International Conference on Electrical & Electronic Engineering (ICEEE) 2017.
- (18) Ghatwai, N. G.; Harpale, V. K.; Kale, M. Vehicle to Vehicle Communication for Crash Avoidance System. *2016 International Conference on Computing Communication Control and automation (ICCUBEA)* 2016.
- (19) Vehicle-to-vehicle communication https://www.nhtsa.gov/ technology-innovation/vehicle-vehicle-communication#nhtsa-inaction (accessed May 10, 2023).
- (20) U.S. Department of Transportation Releases Request for Comment (RFC) on Vehicle-to-Everything (V2X) Communications. https://www. nhtsa.gov/press-releases/us-department-transportation-releasesrequest-comment-rfc-vehicle-everything-v2x. 2018.
- (21) Molesky, S.; Lin, Z.; Piggott, A. Y.; Jin, W.; Vucković, J.; Rodriguez, A. W. Inverse Design in Nanophotonics. *Nat. Photonics* 2018, *12*, 659–670.
- (22) Born, M.; Wolf, E. *Principles of Optics;* Cambridge University Press, 2019, DOI: 10.1017/9781108769914.
- (23) Tikhonravov, A. V.; Trubetskov, M. K.; DeBell, G. W. Application of the Needle Optimization Technique to the Design of Optical Coatings. *Appl. Opt.* 1996, *35*, 5493.
- (24) Rabady, R. I.; Ababneh, A. Global Optimal Design of Optical Multilayer Thin-Film Filters Using Particle Swarm Optimization. *Optik* 2014, *125*, 548–553.
- (25) Schubert, M. F.; Mont, F. W.; Chhajed, S.; Poxson, D. J.; Kim, J. K.; Schubert, E. F. Design of Multilayer Antireflection Coatings Made from Co-Sputtered and Low-Refractive-Index Materials by Genetic Algorithm. *Opt. Express* 2008, *16*, 5290.
- (26) Unni, R.; Yao, K.; Han, X.; Zhou, M.; Zheng, Y. A MixtureDensity-Based Tandem Optimization Network for on-Demand Inverse Design of Thin-Film High Reflectors. *NANO* 2021, *10*, 4057–4065.
- (27) Wang, H.; Guo, L. J. NEUTRON: Neural Particle Swarm Optimization for Material-Aware Inverse Design of Structural Color. *Iscience* 2022, *25*, No. 104339.
- (28) Liu, D.; Tan, Y.; Khoram, E.; Yu, Z. Training Deep Neural Networks for the Inverse Design of Nanophotonic Structures. *ACS Photonics* 2018, *5*, 1365–1369.

- (29) Ma, T.; Tobah, M.; Wang, H.; Guo, L. J.; Department of Physics, The University of Michigan, Ann Arbor, Michigan 48109, USA; Department of Materials Science and Engineering, The University of Michigan, Ann Arbor, Michigan 48109, USA; Department of Electrical Engineering and Computer Science, The University of Michigan, Ann Arbor, Michigan 48109, USA. Benchmarking Deep Learning-Based Models on Nanophotonic
- Inverse Design Problems. *Opto-electronic Sci* 2022, *1*, 210012–210012.
- (30) Jiang, J.; Chen, M.; Fan, J. A. Deep Neural Networks for the Evaluation and Design of Photonic Devices. *Nat. Rev. Mater.* 2021, *6*, 679–700.
- (31) Ma, W.; Liu, Z.; Kudyshev, Z. A.; Boltasseva, A.; Cai, W.; Liu, Y. Deep Learning for the Design of Photonic Structures. *Nat. Photonics* 2021, *15*, 77–90.
- (32) Wang, H.; Zheng, Z.; Ji, C.; Guo, L. J. Automated Multi-Layer Optical Design via Deep Reinforcement Learning. *Mach Learn Sci Technol.* 2021, 2, No. 025013.
- (33) Johnson, P.; Christy, R. Optical Constants of Transition Metals: Ti, V, Cr, Mn, Fe, Co, Ni, and Pd. Phys. Rev. B 1974, 9, 5056–5070.
- (34) Kopas, C. J.; Gonzales, J.; Zhang, S.; Queen, D. R.; Wagner, B.; Robinson, M.; Huffman, J.; Newman, N. Low Microwave Loss in Deposited Si and Ge Thin-Film Dielectrics at Single-Photon Power and Low Temperatures. *Aip Adv* 2021, *11*, No. 095007.
- (35) Balasundaram, N.; Mangalaraj, D.; Narayandass, S. K.; Balasubramanian, C. Structure, Dielectric, and AC Conduction Properties of Amorphous Germanium Thin Films. *Phys. Status Solidi A* 1992, *130*, 141–151.

Recommended by ACS

A Shish-Kebab Superstructure Film for Personal Radiative Cooling

Xianhu Liu, Changyu Shen, et al.

MARCH 22, 2023

ACS APPLIED MATERIALS & INTERFACES

READ 🗹

Simple Template-Mediated Fabrication of ZnO Nanotube Arrays and Their Application in Flexible Ultraviolet Photodetectors

Panpan Chen and Tian Hang

JANUARY 30, 2023

ACS APPLIED NANO MATERIALS

READ

Quasi-Ordered Nanosphere-Based Photonic Crystals with High-Fastness Structural Colors via Screen Printing: Implications for Textile Printing and Dyeing

Xiaodong Lu, Jianzhong Shao, et al.

NOVEMBER 15, 2022

ACS APPLIED NANO MATERIALS

READ C

Amorphous Arrays of Silica Nanoparticles Coated with PDMS Brushes Enable Water-Repellent Noniridescent Structural Colors for Optical Information Encryption

Site Luo, Haihu Yu, et al. JULY 05. 2022

READ 🗹

Get More Suggestions>

ACS APPLIED NANO MATERIALS